

The C^1 Isogeometric analysis procedure for analysis of free vibration of GPLR-FG-TPMS nanoplates embedded in Pasternak foundation

Ngoc-Tu Do^a, Nhan Thinh Hoang^b, Vo Thanh Tuan^{c,*}

^aFaculty of Industrial Systems, School of Mechanical and Automotive Engineering, Hanoi University of Industry, Hanoi, Vietnam. Email: tudn@hau.edu.vn

^bInstitute of International Education, Nguyen Tat Thanh University, Ho Chi Minh City, Vietnam. Email: htghan@ntt.edu.vn

^cInstitute of International Education, Nguyen Tat Thanh University, Ho Chi Minh City, Vietnam. Email: vttuan@ntt.edu.vn

* Corresponding author

Abstract

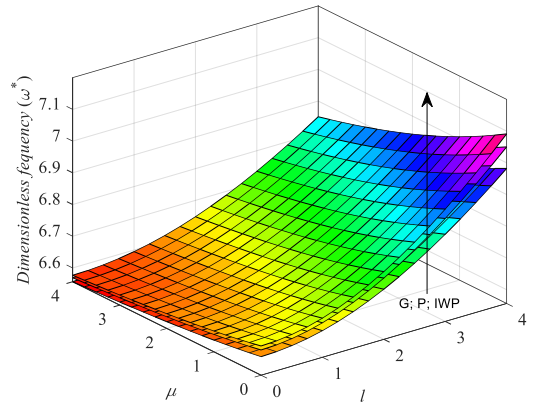
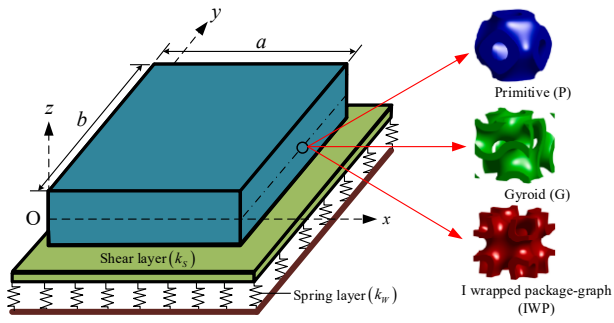
The main goal of this study is to extend the isogeometric analysis (IGA) further to investigate the free vibration of graphene platelet (GPL)-reinforced functionally graded triply periodic minimal surface (FG-TPMS) nanoplates (so-called GPLR-FG-TPMS nanoplates) embedded in Pasternak foundation (PF). The computational model includes both nonlocal elasticity and strain gradient effects to account for the impact of small-size effects inherent in nanostructures. To achieve C^1 -continuity condition, an IGA framework based on HSDT is developed with 7-DOFs per a control point. The motion equation of the nanoplate is derived from Hamilton's principle. The calculation program is coded in Matlab environment and verified through comparative examples. From here, the influence of geometric parameters, material properties, and boundary conditions (BCs) on the frequency of nanoplates is investigated in detail. The results obtained are reference materials for further studies as well as in the calculation and design of GPLR-FG-TPMS structures in practice.

Keywords

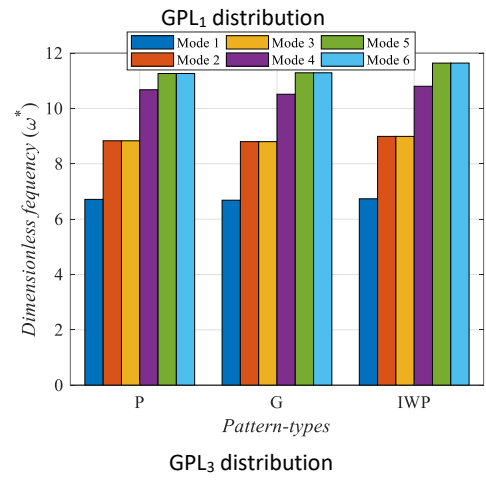
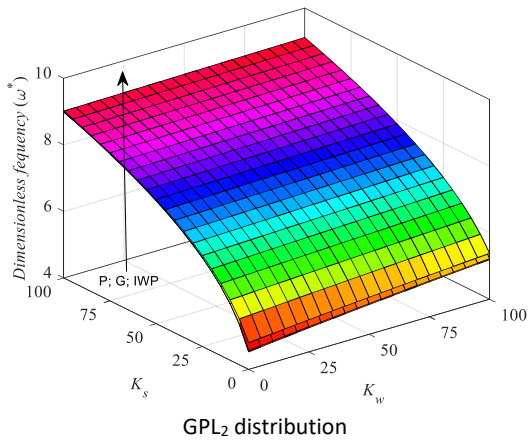
IGA; NSGT; FG-TPMS; elastic foundation; free vibration.

* Corresponding author: vttuan@ntt.edu.vn (Vo Thanh Tuan)

Graphical Abstract

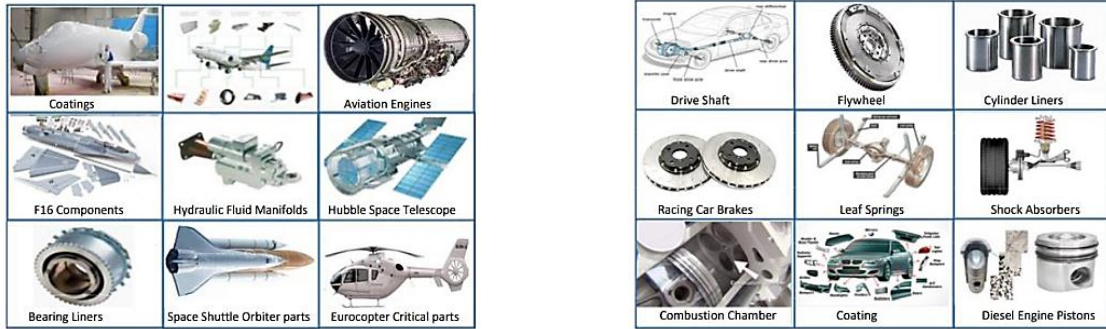


The GPLR-FG-TPMS nanoplatform embedded in PF



1 OVERVIEW OF THE RESEARCH PROBLEM

Graphene platelets (GPLs), a type of nanomaterial, are renowned for their outstanding mechanical, thermal, and electrical properties (Arash & Wang, 2011; Rafiee et al., 2009). It consists of one or more layers of graphene-2D carbon atoms arranged in a hexagonal lattice randomly distributed in the material matrix, which significantly improves the strength of the parent material without much change in the mass of the structure. Therefore, it is increasingly widely applied in various industries, such as aerospace, electronics and energy, defence (Figure 1).



a) GPL-reinforced in aerospace engineering

b) GPL-reinforced in automotive engineering

Figure 1 Applications of GPL in practice (Source: Internet).

As known, TPMS structures are characterized by surfaces that partition space into two equal volumes. The parting surfaces have zero mean curvature, allowing to minimize stresses under the action of loads. TPMS applications span a wide range, as extensively reviewed by Al-Ketan and Abu Al-Rub (2019). Some innovative applications of TPMS structures, readers can refer to the documents (González-Castaño et al., 2022; Singh, Sharma, Kumar, & Vaish, 2023; Zhao, Li, Zhang, & Zhai, 2023). It can be seen that, while many types of TPMS, such as Sankineni and Ravi Kumar (2022), have been studied, the Primitive (P), Gyroid (G), and I-Wrapped Package-Graph (IWP) types are still the most studied and applied. Due to constraints in both computational and experimental aspects, TPMS structures are typically examined at specific levels (Al-Ketan & Abu Al-Rub, 2019). However, for their application in FG structures, it is essential to characterize their mechanical properties across the full relative density range from 0 to 1. To address this, Nguyen-Xuan, Tran, Thai, and Lee (2023) proposed an innovative two-phase function to describe the mechanical behavior of three TPMS types: P, G, and IWP, enabling the advancement of FG-TPMS structures. Building on this foundation, subsequent studies have explored nonlinear behavior in FG-TPMS plates (N. V. Nguyen, Tran, & Nguyen-Xuan, 2024) and size-dependent effects in micro-TPMS plates (N. V. Nguyen, Tran, Phung-Van, Lee, & Nguyen-Xuan, 2023). Various structural analysis methods have been employed, yet since its introduction in 2005 (Hughes, Cottrell, & Bazilevs, 2005), the NURBS-based isogeometric analysis (IGA) has proven to be an effective computational technique for investigating complex structures. For example, Q. H. Nguyen, Nguyen, Nguyen, and Nguyen-Xuan (2020) utilized IGA with a five-variable plate model to examine both closed-cell and TPMS plates. Also using IGA, Ehsan Ansari and Setoodeh (2020); (E Ansari, Setoodeh, & Rabczuk, 2020) conducted vibration analysis of FGM variable-thickness structures. In these studies, he analyzed frequency-locus veering and mode-shape switching of plates.

Microscopic and nanoscopic structures exhibit behaviors that classical plate theory cannot adequately capture, primarily due to the significant influence of small-scale effects on their mechanics. To address these discrepancies, researchers have adopted a dual approach involving experimental studies and computational simulations (Liew, He, & Wong, 2004; Stölken & Evans, 1998). However, the experiments and simulations are only performed on some basic and specific cases. Therefore, it is necessary to establish a suitable theory and model. As a result, several continuum theories have been proposed, including nonlocal elasticity theory (NET) (Eringen, 1972, 1983), nonlocal strain gradient theory (NSGT) (Fleck & Hutchinson, 1993), and modified couple stress theory (MCST) (Toupin, 1962).

Subsequent research has extensively explored the impact of small-scale effects on the mechanical behavior of nanostructures. Among these theories, NET is widely used due to its ability to balance accuracy with mathematical simplicity. For instance, Ahmed Amine Daikh, Draï, Bensaid, Houari, and Tounsi (2021); Ahmed A Daikh and Zenkour (2020) analyzed thermal vibration and bending of FGSW nanoplates under various boundary conditions using analytical methods. Phung-Van, Thai, Abdel-Wahab, and Nguyen-Xuan (2020) optimized FGSW nanoplates through the IGA approach. Arefi and Zenkour (2017) applied a trigonometric plate theory with an exact solution to study the static bending of nanoplates in a multiphysics environment. Li, Lai, and Yang (2019)

combined an exact solution with NET to predict the upper limit of the nonlocal factor in nanostructures. Thai, Ferreira, Nguyen-Xuan, Nguyen, and Phung-Van (2023) utilized the meshfree moving Kriging method with higher-order shape functions to analyze nanoplates. Additionally, Zeighampour and Shojaeian (2019) examined the buckling behavior of micro/nanoshells made of FG material using Donnell shell theory based on MCST, while Li, Zhu, Zhang, Sui, and Zhao (2022) employed NSGT to study the natural frequencies of self-powered nanoribbons.

Although existing studies have applied IGA to a range of problems, its application to the free vibration analysis of GPLR-FG-TPMS nanoplates embedded in PF remains unexplored. To bridge this gap and deepen the understanding of the behavior of GPLR-FG-TPMS nanoplates, this study introduces an efficient IGA approach grounded in HSDT and NSGT. In addition, detailed numerical results are provided to examine the effects of geometrical, material parameters, and BCs on the vibration behavior of GPLR-FG-TPMS nanoplates embedded in PF. The obtained results are expected to be useful for the calculation, design, fabrication, and application of this structure in engineering practice.

2 BASIS FORMULATION

2.1 The nanoplate model

In this paper, considering the GPLR-FG-TPMS nanoplate embedded in PF with different TPMS types: P, G, and IWP as shown in Fig. 2.

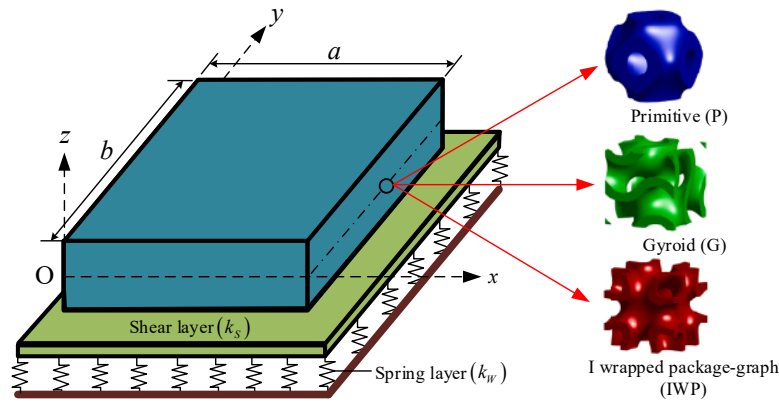


Figure 2 The GPLR-FG-TPMS nanoplate embedded in PF.

The correlation between relative density and elastic characteristics is introduced by (Nguyen-Xuan et al., 2023):

$$\frac{E(z)}{E_s} = \begin{cases} C_1^E \times \rho^{n_1^E} & \rho \leq k_m^E \\ C_2^E \times \rho^{n_2^E} + C_3^E & \rho > k_m^E \end{cases} \quad (1a)$$

$$\frac{G(z)}{G_s} = \begin{cases} C_1^G \times \rho^{n_1^G} & \rho \leq k_m^G \\ C_2^G \times \rho^{n_2^G} + C_3^G & \rho > k_m^G \end{cases} \quad (1b)$$

$$v(z) = \begin{cases} a_1 \times e^{b_1 \times \rho} + d_1 & \rho \leq k_v \\ a_2 \times \rho^2 + b_2 \times \rho + d_2 & \rho > k_v \end{cases} \quad (1c)$$

in which $\rho = \rho(z)/\rho_s$ and other parameters are determined by

$$C_1^E (k_m^E)^{n_1^E} = C_2^E (k_m^E)^{n_2^E} + C_3^E; C_2^E + C_3^E = 1; \quad (2a)$$

$$a_1 e^{b_1 k_v} + d_1 = 0.3; a_2 k_v^2 + b_2 k_v + d_2 = 0.3, a_2 + b_2 + d_2 = 0.3. \quad (2b)$$

with some factors are listed in Table 1.

Table 1 The value of factors in Eq. (1)

Properties	Factor	TPMS types		
		P	G	IWP
E	C_1^E	0.317	0.596	0.597
	n_1^E	2.006	2.351	1.782
	n_2^E	1.715	1.982	2.188
	k_m^E	0.25	0.45	0.35
G	C_1^G	0.705	0.777	0.529
	n_1^G	1.189	1.544	1.287
	n_2^G	1.715	1.982	2.188
	k_m^G	0.25	0.45	0.35
ν	a_1	0.314	0.192	2.597
	b_1	-1.004	-1.349	-0.157
	a_2	0.152	0.402	0.201
	k_ν	0.55	0.50	0.13

The mass density is determined by Nguyen-Xuan et al. (2023):

$$\left\{ \begin{array}{ll} \rho(z) = \rho_s \times \rho_{max} \left[1 - \rho_0 + \rho_0 \times \left(\frac{z}{h} + \frac{1}{2} \right)^{n_1} \right] & \text{PD}_1 \text{ (asymmetric)} \\ \rho(z) = \rho_s \times \rho_{max} \left[1 - \rho_0 + \rho_0 \times \left[1 - \cos \left(\frac{\pi z}{h} \right) \right]^{n_2} \right] & \text{PD}_2 \text{ (symmetric)} \\ \rho(z) = \rho_s \times [1 - g_m \psi_g] & \text{PD}_3 \text{ (uniform)} \end{array} \right. \quad (3)$$

in which $\rho_0 = 1 - \rho_{min}/\rho_{max}$ is the porosity factor; n_1 and n_2 are the power-law indexes of porosity distributions, defined by

$$n_{1,2} = \frac{\rho_{max} - \frac{M}{\rho_s h}}{\frac{M}{\rho_s h} - \rho_{max}(1 - \rho_0)} \quad (4)$$

$$\frac{M}{\rho_s h} = \int_0^{h/2} \frac{\rho_{max} [1 - \rho_0 + \rho_0 \times (1-u)^{n_2}]}{\pi \sqrt{1-u^2}} du \text{ with } u = \cos \left(\frac{\pi z}{h} \right) \quad (5)$$

$$M = \int_{-h/2}^{h/2} \rho(z) dz \quad (6)$$

Three GPL distributions are determined by the function volume fraction $V_r(z)$:

$$\left\{ \begin{array}{ll} V_r^1(z) = S_1 \left[1 - \cos \left(\frac{\pi z}{h} \right) \right] & \text{GPL}_1 \text{ (symmetric)} \\ V_r^2(z) = S_2 \left[1 - \cos \left(\frac{\pi z}{2h} + \frac{\pi}{4} \right) \right] & \text{GPL}_2 \text{ (asymmetric)} \\ V_r^3(z) = S_3 & \text{GPL}_3 \text{ (uniform)} \end{array} \right. \quad (7)$$

herein S_1 , S_2 , and S_3 are the maximum of GPL volume fractions:

$$S_i = \frac{V_r^{total} \int_{-h/2}^{h/2} \rho(z)/\rho_s dz}{\int_{-h/2}^{h/2} V_r^i(z)/S_i \times \rho(z)/\rho_s dz} \quad (8)$$

with

$$V_r^{total} = \frac{\Lambda_r \rho_m}{\Lambda_r \rho_m + \rho_r - \Lambda_r \rho_r} \quad (9)$$

where Λ_r signifies the GPL's weight fraction.

The effective elastic modulus following the Halpin-Tsai model is:

$$E_s = \left[\frac{3}{8} \frac{1 + \xi_L \eta_L V_r}{1 - \eta_L V_r} + \frac{5}{8} \frac{1 + \xi_w \eta_w V_r}{1 - \eta_w V_r} \right] E_m \quad (10)$$

in which ξ_L , η_L , ξ_w , and η_w parameters are calculated by

$$\eta_L = \frac{E_r/E_m - 1}{E_r/E_m + \xi_L}, \eta_w = \frac{E_r/E_m - 1}{E_r/E_m + \xi_w}, \xi_L = \frac{2l_r}{t_r}, \xi_w = \frac{2w_r}{t_r} \quad (11)$$

The effective Poisson's ratio and the mass density according to the rule of mixtures are:

$$v_s = v_m V_m + v_r V_r \quad (12)$$

$$\rho_s = \rho_m V_m + \rho_r V_r \quad (13)$$

In this study, the PF model is used with foundation reaction given by Keshtegar, Motezaker, Kolahchi, and Trung (2020):

$$\mathcal{R} = k_w w(x, y) - k_s \left(\left(\frac{\partial w}{\partial x} \right)^2 + \left(\frac{\partial w}{\partial y} \right)^2 \right) \quad (14)$$

where k_w and k_s denote spring stiffness and shear stiffness.

2.2 Nonlocal strain gradient theory

The governing equation in partial differential form following NSGT is expressed by (Lim, Zhang, & Reddy, 2015; Lu, Zhang, Lee, Wang, & Reddy, 2007; Soldatos, 1992; Thai, Ferreira, & Phung-Van, 2020):

$$\sigma_{ij,j} - \lambda \nabla^2 \sigma_{ij,j} + (1 - \mu \nabla^2) f_i = (1 - \mu \nabla^2) \rho \ddot{u}_i \quad (15)$$

where σ_{ij} is the local linear stress tensor associated with the classical continuum theory; $\nabla^2 = \frac{\partial^2}{\partial x^2} + \frac{\partial^2}{\partial y^2}$ is Laplace operator; μ and $\lambda = \ell^2$ are the parameters of the nonlocal and length scale terms, respectively.

The weak form equation in the form of Hamilton's principle is defined by Li et al. (2022):

$$\int_{t_0}^{t_1} \left[\int_V (\sigma_{ij} - \lambda \nabla^2 \sigma_{ij}) \delta \varepsilon_{ij} dV + \int_V (1 - \mu \nabla^2) \rho \ddot{u}_i \delta u_i dV - \int_V (1 - \mu \nabla^2) f_i \delta u_i dV \right] dt = 0 \quad (16)$$

with t_0 and t_1 being the initial and final times of the simulation or physical process, their role is clearly defining the time domain over which the weak form is valid. Impose the temporal boundary condition $\delta u_i(t_0) = \delta u_i(t_1) = 0$ for all spatial points in the domain V , ensuring consistency with the variational formulation.

2.3 Displacement field of plates based on HSDT

The displacement field based on HSDT is given by Soldatos (1992):

$$\mathbf{u}(x, y, z) = \mathbf{u}_0(x, y) + z \mathbf{u}_1(x, y) + f(z) \mathbf{u}_2(x, y) \quad (17)$$

where

$$\mathbf{u} = \begin{Bmatrix} u \\ v \\ w \end{Bmatrix}, \mathbf{u}_0 = \begin{Bmatrix} u_0 \\ v_0 \\ w_0 \end{Bmatrix}, \mathbf{u}_1 = \begin{Bmatrix} -\beta_x \\ -\beta_y \\ 0 \end{Bmatrix}, \mathbf{u}_2 = \begin{Bmatrix} \theta_x \\ \theta_y \\ 0 \end{Bmatrix} \quad (18)$$

with $u_0, v_0, w_0, \beta_x = w_{0,x}, \beta_y = w_{0,y}, \theta_x$, and θ_y are the displacement variables. The transverse shear function $f(z) = h \sinh(z/h) - z \cosh(1/2)$.

Now, the strain field is determined by Reddy (1984):

$$\{\varepsilon_{xx}, \varepsilon_{yy}, \gamma_{xy}\}^T = \varepsilon_0 + z \varepsilon_1 + f(z) \varepsilon_2; \quad (19a)$$

$$\{\gamma_{xz}, \gamma_{yz}\}^T = \varepsilon_{s0} + f'(z) \varepsilon_{s1} \quad (19b)$$

in which

$$\varepsilon_0 = \begin{Bmatrix} u_{0,x} \\ v_{0,y} \\ u_{0,y} + v_{0,x} \end{Bmatrix}; \varepsilon_1 = - \begin{Bmatrix} \beta_{x,x} \\ \beta_{y,y} \\ \beta_{x,y} + \beta_{y,x} \end{Bmatrix}; \varepsilon_2 = \begin{Bmatrix} \theta_{x,x} \\ \theta_{y,y} \\ \theta_{y,x} + \theta_{x,y} \end{Bmatrix}; \quad (20a)$$

$$\varepsilon_{s0} = \begin{Bmatrix} w_{0,x} - \beta_x \\ w_{0,y} - \beta_y \end{Bmatrix}; \varepsilon_{s1} = \begin{Bmatrix} \theta_x \\ \theta_y \end{Bmatrix}. \quad (20b)$$

The stress-strain relationship is determined by Hooke's law as follows (Reddy, 1984):

$$\begin{Bmatrix} \sigma_{xx} \\ \sigma_{yy} \\ \tau_{xy} \\ \tau_{xz} \\ \tau_{yz} \end{Bmatrix} = \begin{bmatrix} C_{11} & C_{12} & 0 & 0 & 0 \\ C_{21} & C_{22} & 0 & 0 & 0 \\ 0 & 0 & C_{66} & 0 & 0 \\ 0 & 0 & 0 & C_{55} & 0 \\ 0 & 0 & 0 & 0 & C_{44} \end{bmatrix} \begin{Bmatrix} \varepsilon_{xx} \\ \varepsilon_{yy} \\ \gamma_{xy} \\ \gamma_{xz} \\ \gamma_{yz} \end{Bmatrix} \quad (21)$$

where C_{ij} refers to the elastic coefficients which can be evaluated through effective material properties Young's modulus $E(z)$, shear modulus $G(z)$, and Poisson's ratio $\nu(z)$ may vary through the thickness and are expressed as following:

$$C_{11} = C_{22} = \frac{E(z)}{1 - \nu(z)^2}; C_{12} = C_{21} = \frac{\nu(z)E(z)}{1 - \nu(z)^2}; C_{44} = C_{55} = C_{66} = G(z) \quad (22)$$

2.4 Weak form

Substituting Eqs. (19) and (21) into Eq. (16), the weak form of the governing equation of free vibration of plates resting on PF is as follows:

$$\delta \int_{t_0}^{t_1} \int_{\Omega} \left[\frac{1}{2} \hat{\boldsymbol{\varepsilon}}^T \mathbb{D}_b \hat{\boldsymbol{\varepsilon}} + \frac{1}{2} \boldsymbol{\gamma}^T \mathbb{D}_s \boldsymbol{\gamma} - \frac{\lambda}{2} (\nabla^2 \hat{\boldsymbol{\varepsilon}})^T \mathbb{D}_b \hat{\boldsymbol{\varepsilon}} + \frac{\lambda}{2} (\nabla^2 \boldsymbol{\gamma})^T \mathbb{D}_s \boldsymbol{\gamma} + \frac{1}{2} (1 - \mu \nabla^2) \hat{\mathbf{u}}^T \mathbb{m} \hat{\mathbf{u}} - (1 - \mu \nabla^2) \mathcal{R} w \right] d\Omega dt = 0. \quad (23a)$$

Applying the first variation of this action, we obtain:

$$\int_{\Omega} \delta \hat{\boldsymbol{\varepsilon}}^T \mathbb{D}_b \hat{\boldsymbol{\varepsilon}} d\Omega - \lambda \int_{\Omega} \delta (\nabla^2 \hat{\boldsymbol{\varepsilon}})^T \mathbb{D}_b \hat{\boldsymbol{\varepsilon}} d\Omega + \int_{\Omega} \delta \boldsymbol{\gamma}^T \mathbb{D}_s \boldsymbol{\gamma} d\Omega - \lambda \int_{\Omega} \delta (\nabla^2 \boldsymbol{\gamma})^T \mathbb{D}_s \boldsymbol{\gamma} d\Omega + \int_{\Omega} (1 - \mu \nabla^2) \mathcal{R} \delta w d\Omega + \int_{\Omega} (1 - \mu \nabla^2) \delta \hat{\mathbf{u}}^T \mathbb{m} \hat{\mathbf{u}} d\Omega = 0. \quad (23b)$$

where

$$\hat{\boldsymbol{\varepsilon}} = \begin{Bmatrix} \varepsilon_0 \\ \varepsilon_1 \\ \varepsilon_2 \end{Bmatrix}, \boldsymbol{\gamma} = \begin{Bmatrix} \varepsilon_{s0} \\ \varepsilon_{s1} \end{Bmatrix}, \mathbb{D}_b = \begin{bmatrix} \mathbb{A} & \mathbb{B} & \mathbb{H} \\ \mathbb{B} & \mathbb{D} & \mathbb{F} \\ \mathbb{H} & \mathbb{F} & \mathbb{L} \end{bmatrix}, \mathbb{D}_s = \begin{bmatrix} \mathbb{A}^s & \mathbb{B}^s \\ \mathbb{B}^s & \mathbb{C}^s \end{bmatrix} \quad (24)$$

with

$$(\mathbb{A}, \mathbb{B}, \mathbb{D}, \mathbb{H}, \mathbb{F}, \mathbb{L}) = \int_{-\frac{h}{2}}^{\frac{h}{2}} (1, z, z^2, f(z), zf(z), f^2(z)) \begin{bmatrix} C_{11} & C_{12} & 0 \\ C_{21} & C_{22} & 0 \\ 0 & 0 & C_{66} \end{bmatrix} dz; \quad (25a)$$

$$(\mathbb{A}^s, \mathbb{B}^s, \mathbb{C}^s) = \int_{-\frac{h}{2}}^{\frac{h}{2}} (1, f'(z), f'^2(z)) \begin{bmatrix} C_{55} & 0 \\ 0 & C_{44} \end{bmatrix} dz. \quad (25b)$$

and

$$\mathbb{m} = \begin{bmatrix} \boldsymbol{\ell}_1 & \boldsymbol{\ell}_2 & \boldsymbol{\ell}_4 \\ \boldsymbol{\ell}_2 & \boldsymbol{\ell}_3 & \boldsymbol{\ell}_5 \\ \boldsymbol{\ell}_4 & \boldsymbol{\ell}_5 & \boldsymbol{\ell}_6 \end{bmatrix}, \hat{\mathbf{u}} = \begin{Bmatrix} \mathbf{u}_0 \\ \mathbf{u}_1 \\ \mathbf{u}_2 \end{Bmatrix} \quad (26)$$

in which

$$(\boldsymbol{\ell}_1, \boldsymbol{\ell}_2, \boldsymbol{\ell}_3, \boldsymbol{\ell}_4, \boldsymbol{\ell}_5, \boldsymbol{\ell}_6) = \mathbf{I}_{3 \times 3} \int_{-h/2}^{h/2} \rho(1, z, z^2, f(z), zf(z), f^2(z)) dz \quad (27)$$

3 THE IGA PROCEDURE

The displacement field following NURBS functions is introduced by Tran, Hoang, Lee, and Nguyen-Xuan (2024):

$$\mathbf{u}^h(\xi, \eta) = \sum_{I=1}^{n \times m} \mathbf{I}_7 N_I(\xi, \eta) \mathbf{q}_I \quad (28)$$

here, the displacement vector corresponding to control point I is expressed as $\mathbf{q}_I = \{u_{0I} \ v_{0I} \ w_I \ \theta_{xI} \ \theta_{yI} \ \beta_{xI} \ \beta_{yI}\}^T$. The matrix \mathbf{I}_7 is a 7×7 identity matrix, where n and m denote the total number of control points.

Now, the strain-displacement relation is defined by

$$\hat{\boldsymbol{\varepsilon}} = \{\varepsilon_0 \ \varepsilon_1 \ \varepsilon_2\}^T = \sum_{I=1}^{n \times m} [\mathbf{B}_I^0 \ \mathbf{B}_I^1 \ \mathbf{B}_I^2]^T \mathbf{q}_I = \sum_{I=1}^{n \times m} \bar{\mathbf{B}}_I^b \mathbf{q}_I \quad (29a)$$

$$\gamma = \{\varepsilon_{s0} \quad \varepsilon_{s1}\}^T = \sum_{l=1}^{n \times m} [\mathbf{B}_l^{s0} \quad \mathbf{B}_l^{s1}]^T \mathbf{q}_l = \sum_{l=1}^{n \times m} \bar{\mathbf{B}}_l^s \mathbf{q}_l \quad (29b)$$

where

$$\mathbf{B}_l^0 = \begin{bmatrix} N_{l,x} & 0 & 0 & 0 & 0 & 0 & 0 \\ 0 & N_{l,y} & 0 & 0 & 0 & 0 & 0 \\ N_{l,y} & N_{l,x} & 0 & 0 & 0 & 0 & 0 \end{bmatrix}; \quad (30a)$$

$$\mathbf{B}_l^1 = - \begin{bmatrix} 0 & 0 & 0 & 0 & 0 & N_{l,x} & 0 \\ 0 & 0 & 0 & 0 & 0 & 0 & N_{l,y} \\ 0 & 0 & 0 & 0 & 0 & N_{l,y} & N_{l,x} \end{bmatrix}; \quad (30b)$$

$$\mathbf{B}_l^2 = \begin{bmatrix} 0 & 0 & 0 & N_{l,x} & 0 & 0 & 0 \\ 0 & 0 & 0 & 0 & N_{l,y} & 0 & 0 \\ 0 & 0 & 0 & N_{l,y} & N_{l,x} & 0 & 0 \end{bmatrix}; \quad (30c)$$

$$\mathbf{B}_l^{s0} = \begin{bmatrix} 0 & 0 & N_{l,x} & 0 & 0 & -N_l & 0 \\ 0 & 0 & N_{l,y} & 0 & 0 & 0 & -N_l \end{bmatrix}; \quad (30d)$$

$$\mathbf{B}_l^{s1} = \begin{bmatrix} 0 & 0 & 0 & N_l & 0 & 0 & 0 \\ 0 & 0 & 0 & N_l & 0 & 0 & 0 \end{bmatrix}. \quad (30e)$$

Alternatively, the displacement field is determined by

$$\hat{\mathbf{u}} = \{\mathbf{u}_0 \quad \mathbf{u}_1 \quad \mathbf{u}_2\}^T = \sum_{l=1}^{n \times m} [\mathbf{N}_l^0 \quad \mathbf{N}_l^1 \quad \mathbf{N}_l^2]^T \mathbf{q}_l = \sum_{l=1}^{n \times m} \bar{\mathbf{N}}_l \mathbf{q}_l \quad (31)$$

with

$$\mathbf{N}_l^0 = \begin{bmatrix} N_l & 0 & 0 & 0 & 0 & 0 & 0 \\ 0 & N_l & 0 & 0 & 0 & 0 & 0 \\ 0 & 0 & N_l & 0 & 0 & 0 & 0 \end{bmatrix}; \quad (32a)$$

$$\mathbf{N}_l^1 = - \begin{bmatrix} 0 & 0 & 0 & 0 & 0 & N_l & 0 \\ 0 & 0 & 0 & 0 & 0 & 0 & N_l \\ 0 & 0 & 0 & 0 & 0 & 0 & 0 \end{bmatrix}; \quad (32b)$$

$$\mathbf{N}_l^2 = \begin{bmatrix} 0 & 0 & 0 & N_l & 0 & 0 & 0 \\ 0 & 0 & 0 & 0 & N_l & 0 & 0 \\ 0 & 0 & 0 & 0 & 0 & 0 & 0 \end{bmatrix}. \quad (32c)$$

Substituting Eqs. (30) and (31) into Eq. (23), the motion equation of the nanoplate is:

$$\mathbf{M}\dot{\mathbf{q}} + (\mathbf{K} + \mathbf{K}^f)\mathbf{q} = \mathbf{0} \quad (33)$$

in which

The stiffness matrix:

$$\begin{aligned} \mathbf{K} = & \int_{\Omega} (\bar{\mathbf{B}}^b)^T \hat{\mathbf{D}}^b \bar{\mathbf{B}}^b d\Omega + \int_{\Omega} (\bar{\mathbf{B}}^s)^T \hat{\mathbf{D}}^s \bar{\mathbf{B}}^s d\Omega - \lambda \int_{\Omega} (\nabla^2 \bar{\mathbf{B}}^b)^T \hat{\mathbf{D}}^b \bar{\mathbf{B}}^b d\Omega \\ & - \lambda \int_{\Omega} (\nabla^2 \bar{\mathbf{B}}^s)^T \hat{\mathbf{D}}^s \bar{\mathbf{B}}^s d\Omega \end{aligned} \quad (34)$$

The foundation stiffness matrix:

$$\begin{aligned}
\mathbf{K}^f = k_w \int_{\Omega} \left[(\mathbf{N}_I^w)^T (\mathbf{N}_I^w) + \mu \left[(\mathbf{N}_{I,x}^w)^T (\mathbf{N}_{I,x}^w) + (\mathbf{N}_{I,y}^w)^T (\mathbf{N}_{I,y}^w) \right] \right] d\Omega \\
+ k_s \int_{\Omega} \left[(\mathbf{N}_{I,x}^w)^T (\mathbf{N}_{I,x}^w) + (\mathbf{N}_{I,y}^w)^T (\mathbf{N}_{I,y}^w) \right. \\
\left. + \mu \left[(\mathbf{N}_{I,xx}^w)^T (\mathbf{N}_{I,xx}^w) + (\mathbf{N}_{I,yy}^w)^T (\mathbf{N}_{I,yy}^w) \right] \right] d\Omega
\end{aligned} \tag{35}$$

with

$$\mathbf{N}_I^w = \sum_{l=1}^{n \times m} [0 \quad 0 \quad N_l \quad 0 \quad 0 \quad 0 \quad 0]; \tag{36a}$$

$$\mathbf{N}_{I,x}^w = \sum_{l=1}^{n \times m} [0 \quad 0 \quad N_{l,x} \quad 0 \quad 0 \quad 0 \quad 0]; \tag{36b}$$

$$\mathbf{N}_{I,y}^w = \sum_{l=1}^{n \times m} [0 \quad 0 \quad N_{l,y} \quad 0 \quad 0 \quad 0 \quad 0]. \tag{36c}$$

The mass matrix:

$$\mathbf{M} = \int_{\Omega} (1 - \mu \nabla^2) \bar{\mathbf{N}}^T \mathbf{I} \bar{\mathbf{N}} d\Omega. \tag{37}$$

The BCs are used in this study, introduced by

- Clamped (C):

$$u_0 = v_0 = w_0 = \beta_x = \beta_y = \theta_x = \theta_y = 0.$$

- Simply supported (S):

$$u_0 = w_0 = \beta_x = \theta_x = 0 \text{ at } y = 0 \text{ \& } y = b.$$

$$v_0 = w_0 = \beta_y = \theta_y = 0 \text{ at } x = 0 \text{ \& } x = a.$$

4 NUMERICAL RESULTS

This section fully studies the natural frequencies of GPLR-FG-TPMS nanoplates with various input parameters. IGA framework uses third-order NURBS elements with a uniform mesh grid. The mechanical properties of the components are presented in Table 2. The basic geometric dimensions of the GPL are $wr = 1.5 \mu\text{m}$, $lr = 2.5 \mu\text{m}$, $tr = 1.5 \text{ nm}$.

The dimensionless parameters are introduced by

$$K_w = k_w \frac{a^4}{D_s}; K_s = k_s \frac{a^2}{D_s} \text{ with } D_s = \frac{E_s h^3}{12(1-\nu_s^2)}; \omega^* = \sqrt[4]{\frac{\omega^2 \rho_s a^4 h}{D_s}}. \tag{38}$$

Table 2 The fundamental mechanical material properties

Material	Young's Modulus (GPa)	Poisson's Ratio	Density (kg/m ³)
Si3N4	348.43	0.3	2370
SUS304(2)	201.04	0.24	8166
GPL	1010	0.186	1062.5
Copper	130	0.34	8960
SUS304	200	0.3	8000

4.1 Verification studies

Firstly, let's consider the SSSS FG-TPMS square plates. Table 3 provides the dimensionless fundamental frequency of plates with different mesh sizes. Noting that the obtained results stabilize at a 9×9 mesh grid and align closely with those of Tran et al. (2024), who employed IGA based on HSDT with five degrees of freedom per point, the 9×9 mesh grid is selected for subsequent examples.

Secondly, the dimensionless frequencies $\Omega = 10\omega h \sqrt{\rho_m/E_m}$ of SSSS FGM (Si₃N₄/SUS304-2) square nanoplate in this study are used for comparison purposes with the results of Sobhy and Radwan (2017) using an exact solution based on Quasi-3D theory and Ahmed A Daikh and Zenkour (2020) employing a closed formulation based on HSDT are provided in Table 4. Observing that the obtained frequency is slightly smaller than the reference frequency. The decreasing difference corresponds to larger nonlocal factor μ and thinner nanoplates. From the above two examples, the correctness of the proposed method can be confirmed.

Table 3 The dimensionless fundamental frequency of FG-TPMS (SUS304) plates with $a/h = 10$ ($\rho_{max} = 1$, $M/(\rho_s h) = 0.35$, and $\Lambda_{GPL} = 0$ wt.%)

TPMS types	Mesh grid	$\rho_0 = 0.75$		$\rho_0 = 0.85$		$\rho_0 = 0.95$	
		PD ₁	PD ₂	PD ₁	PD ₂	PD ₁	PD ₂
P	5 × 5	3.7053	4.1912	3.4545	4.3888	3.1585	4.4558
	7 × 7	3.7052	4.1911	3.4544	4.3887	3.1584	4.4558
	9 × 9	3.7052	4.1911	3.4544	4.3887	3.1584	4.4558
	11 × 11	3.7052	4.1911	3.4544	4.3887	3.1584	4.4558
	13 × 13	3.7052	4.1911	3.4544	4.3887	3.1584	4.4558
	Tran et al. (2024)	3.7051	4.1936	3.4543	4.3894	3.1584	4.4619
G	5 × 5	3.6611	4.0849	3.3617	4.2469	3.0434	4.3005
	7 × 7	3.6610	4.0848	3.3616	4.2468	3.0433	4.3005
	9 × 9	3.6610	4.0848	3.3616	4.2468	3.0433	4.3005
	11 × 11	3.6610	4.0848	3.3616	4.2468	3.0433	4.3005
	13 × 13	3.6610	4.0848	3.3616	4.2468	3.0433	4.3005
	Tran et al. (2024)	3.6608	4.0872	3.3614	4.2496	3.0432	4.3135
IWP	5 × 5	3.7604	4.1446	3.5141	4.3021	3.2079	4.3472
	7 × 7	3.7603	4.1445	3.5140	4.3020	3.2078	4.3472
	9 × 9	3.7603	4.1445	3.5140	4.3020	3.2078	4.3472
	11 × 11	3.7603	4.1445	3.5140	4.3020	3.2078	4.3472
	13 × 13	3.7603	4.1445	3.5140	4.3020	3.2078	4.3472
	Tran et al. (2024)	3.7602	4.1469	3.5139	4.3042	3.2076	4.3584

Table 4 The dimensionless frequencies Ω of SSSS FGM square nanoplates

h/a	μ	$n = 1$			$n = 5$		
		Sobhy and Radwan (2017)	Ahmed A Daikh and Zenkour (2020)	Present	Sobhy and Radwan (2017)	Ahmed A Daikh and Zenkour (2020)	Present
0.1	0	0.82250	0.82296	0.81658	0.66485	0.66510	0.65828
	0.5 ²	0.80292	0.80338	0.79715	0.64903	0.64927	0.64262
	1	0.75165	0.75208	0.74624	0.60758	0.60781	0.60158
	1.5 ²	0.68443	0.68483	0.67951	0.55325	0.55346	0.54778
	2 ²	0.61484	0.61520	0.61041	0.49699	0.49719	0.49208
0.05	0	0.21083	0.21098	0.20921	0.17077	0.17086	0.16888
	0.5 ²	0.20581	0.20596	0.20423	0.16671	0.16679	0.16486
	1	0.19267	0.19280	0.19119	0.15606	0.15614	0.15434
	1.5 ²	0.17544	0.17556	0.17409	0.14210	0.14218	0.14053
	2 ²	0.15760	0.15771	0.15639	0.12765	0.12772	0.12624

4.2 Free vibration problem

This part investigates the impact of different input parameters on the free vibration of GPLR-FG-TPMS square nanoplates made of copper (Cu) with the given parameters: $a = b = 10$, $\rho_{max} = 1$, and $M/(\rho_s h) = 0.35$.

Firstly, Figure 3 presents the first six mode shapes of SSSS GPLR-FG-TPMS square nanoplates. It can be seen that mode 2 and mode 3 as well as mode 5 and mode 6 have the same shape (equal frequency), only differing in viewing direction due to the symmetrical plate with S boundary at four edges. In addition, Table 5 also provides the first six dimensionless frequency SSSS square nanoplates with different patterns, GPL and PDs distributions. The results show the simultaneous impact of these parameters on the natural frequencies of the nanoplates. The individual frequencies have different values for each distribution, so they affect the effective material properties Young's modulus $E(z)$, shear modulus $G(z)$, and Poisson's ratio $\nu(z)$ of the nanoplates.

Secondly, the combined impact of various input parameters on the dimensionless fundamental frequency of square nanoplates is presented in Tables 6 and 7. Across all nanoplate configurations, we observe the expected trend: as the value of μ increases, the fundamental frequency decreases. The stiffness-softening

mechanism inherent in small-scale structures becomes more pronounced as the nonlocal factor μ increases. On the other hand, as the value of l increases, the fundamental frequency also rises, aligning with expectations. These findings demonstrate that tuning the length scale l provides a means to observe the stiffness-hardening behavior in small-scale plates. Additionally, the PD₂ porosity distribution (symmetric) leads to the highest fundamental frequency, whereas the PD₁ and PD₃ distributions show almost the same frequency. The simultaneous effect of these two parameters on the frequency of the plate can be observed more clearly in Figures 4 and 5. Besides, it is observed that nanoplates with P and IWP types have higher frequencies than nanoplates with G type.

Thirdly, Figures 6, 7 and 8 present the effect of elastic foundation on the fundamental frequency of square nanoplates. Observing that the increase of K_w and K_s leads to an increase in the fundamental frequency of the plate, however, the increase of K_s leads to a faster increase in frequency than the increase of K_w . It can be affirmed that the shear layer supports more effectively than the spring layer. In this investigation, the nanoplate with IWP type resulted in the largest frequency, while the nanoplate with G and P types resulted in approximately the same frequencies.

Next, Figures 9, 10 and 11 illustrate the contrasting effects of the porosity factor ρ_0 on the fundamental natural frequencies of square nanoplates for different GPL distributions. As ρ_0 increases, the mechanical responses of PD₁ and PD₂ distributions diverge completely. Specifically, a higher ρ_0 results in a decrease in the fundamental frequency of PD₁ distribution while it increases the fundamental frequency for PD₂ distribution. Besides, the nanoplates with PD₃ distribution have constant frequency with the change of ρ_0 . Additionally, the nanoplates with the IWP type exhibit the highest frequencies, whereas G type structures demonstrate the lowest performance. Observing Figures 9a, 10a, and 11a, we see that when the porosity factor $\rho_0 = 0.8$, the natural frequencies corresponding to both P type and G type are nearly identical. This suggests that at this intermediate density level, the influence of geometric configuration on the vibration behavior is comparable for both types. However, a clear trend emerges outside this point: when $\rho_0 > 0.8$, the frequency associated with the P type becomes higher than that of the G type, whereas for $\rho_0 < 0.8$, the G type exhibits a higher frequency than the P type. This behavior indicates a nonlinear dependence of the natural frequency on both material distribution and structural geometry. Specifically, at lower densities ($\rho_0 < 0.8$), the G type may distribute material more efficiently, resulting in relatively higher stiffness and, consequently, higher frequency. On the other hand, at higher densities ($\rho_0 > 0.8$), the P type may better utilize the added material to enhance stiffness, leading to a higher natural frequency. Although the frequency difference between the two types remains relatively small across the density range, this trend highlights the significant role of structural geometry in tailoring the vibration behavior of porous or architected materials. Such insights are particularly valuable in the optimal design of lightweight materials where both stiffness and dynamic performance are critical, as in aerospace, automotive, and structural engineering applications.

Additionally, we study the impact of GPL distribution on fundamental frequencies of square nanoplates. Figure 12 highlights the significant impact of both GPL distribution and weight fraction Λ_{GPL} on frequencies of nanoplates. The addition of the reinforcement phase to the metal matrix material clearly results in a significant improvement in overall stiffness. Moreover, the most effective reinforcement configuration is attained by combining the IWP type with GPL₁ distribution. Conversely, the nanoplate with G type and GPL₂ distribution exhibits the lowest frequency. When evaluating the effectiveness of GPL dispersion throughout the thickness of each TPMS structure, the GPL₁ shows the most effective reinforcement, followed by GPL₂ and GPL₃ distributions.

Finally, Figures 13 and 14 show the first six fundamental frequencies of SSSS nanoplates with PD₁ and PD₂ distributions. It is observed that the 2nd and 3rd as well as the 5th and 6th frequencies are equal. This is because the square nanoplate is subjected to the same simply supported on all four edges, the natural vibration modes corresponding to these frequencies differ only in the viewing direction.

Table 5 The first six dimensionless frequency SSSS square nanoplates with different pattern types, GPL and PD distributions ($a/h = 40$, $K_w = 25$, $K_s = 25$, $\rho_0 = 0.85$, $\mu = l = 1$, and $\Lambda_{GPL} = 1$ wt.%)

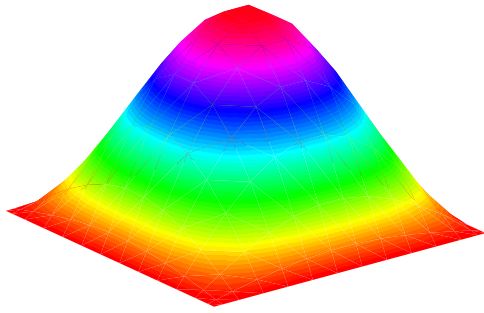
Pattern types	Frequencies	PD ₁			PD ₂			PD ₃		
		GPL ₁	GPL ₂	GPL ₃	GPL ₁	GPL ₂	GPL ₃	GPL ₁	GPL ₂	GPL ₃
P	ω_1^*	6.5048	6.4759	6.4961	6.8709	6.8175	6.8287	6.5525	6.5179	6.5179
	ω_2^*	8.4141	8.3461	8.3943	9.0049	8.9628	8.941	8.5408	8.4574	8.4574
	ω_3^*	8.4141	8.3461	8.3943	9.0049	8.9628	8.941	8.5408	8.4574	8.4574
	ω_4^*	8.9944	8.9922	8.9285	9.0238	8.9816	8.9598	8.5524	8.5524	8.5502
	ω_5^*	8.9944	8.9922	8.9285	9.0238	8.9816	8.9598	8.5524	8.5524	8.5502
	ω_6^*	9.0132	9.011	8.9472	9.3102	9.1916	9.217	8.5703	8.5703	8.5681
G	ω_1^*	6.4853	6.4602	6.4783	6.8365	6.7858	6.7964	6.5343	6.5021	6.5021
	ω_2^*	8.4059	8.3399	8.3871	8.6277	8.5588	8.5255	7.9607	7.9607	7.9586
	ω_3^*	8.4059	8.3399	8.3871	8.6277	8.5588	8.5255	7.9607	7.9607	7.9586
	ω_4^*	8.6092	8.6093	8.5073	8.6458	8.5768	8.5433	7.9774	7.9774	7.9753
	ω_5^*	8.6092	8.6093	8.5073	8.6458	8.5768	8.5433	7.9774	7.9774	7.9753
	ω_6^*	8.6272	8.6273	8.5251	9.2445	9.1328	9.1572	8.5248	8.4426	8.4426
IWP	ω_1^*	6.5232	6.4914	6.5131	6.8649	6.8133	6.8242	6.5519	6.5175	6.5175
	ω_2^*	8.5244	8.4398	8.4348	8.5529	8.4876	8.4557	7.7358	7.7358	7.7338
	ω_3^*	8.5244	8.4398	8.4348	8.5529	8.4876	8.4557	7.7358	7.7358	7.7338
	ω_4^*	8.5408	8.5318	8.4525	8.5708	8.5054	8.4734	7.752	7.752	7.750
	ω_5^*	8.5408	8.5318	8.4525	8.5708	8.5054	8.4734	7.752	7.752	7.750
	ω_6^*	8.5587	8.5497	8.497	9.331	9.2185	9.2437	8.5995	8.5087	8.5088

Table 6 The effect of the nonlocal factor on dimensionless fundamental frequency SSSS square nanoplates with different pattern types, GPL and porosity distributions ($a/h = 15$, $K_w = 100$, $K_s = 50$, $\rho_0 = 0.7$, $l = 1$, and $\Lambda_{GPL} = 1$ wt.%)

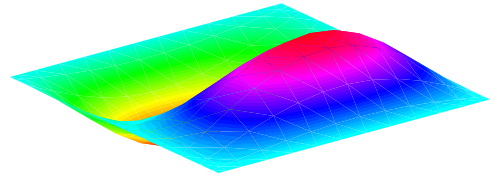
Nonlocal factor (μ)	Pattern types	PD ₁			PD ₂			PD ₃		
		GPL ₁	GPL ₂	GPL ₃	GPL ₁	GPL ₂	GPL ₃	GPL ₁	GPL ₂	GPL ₃
0	P	7.8441	7.7807	7.8062	7.9227	7.8431	7.8566	7.8015	7.752	7.7584
	G	7.829	7.7701	7.7932	7.8966	7.8243	7.8367	7.7849	7.7394	7.7455
	IWP	7.8505	7.7881	7.8121	7.917	7.8424	7.8552	7.7994	7.7513	7.7577
1	P	7.8031	7.7487	7.7709	7.8706	7.8023	7.8142	7.7675	7.7252	7.7310
	G	7.7903	7.7398	7.7600	7.8485	7.7864	7.7973	7.7535	7.7146	7.7200
	IWP	7.8086	7.7551	7.7761	7.8659	7.8017	7.8131	7.7658	7.7247	7.7303
2	P	7.7732	7.7254	7.7453	7.8326	7.7725	7.7833	7.7428	7.7058	7.7110
	G	7.7621	7.7177	7.7359	7.8133	7.7587	7.7687	7.7307	7.6966	7.7016
	IWP	7.7781	7.7311	7.7498	7.8285	7.7721	7.7824	7.7413	7.7053	7.7105
4	P	7.7325	7.6937	7.7105	7.7807	7.732	7.7413	7.7093	7.6795	7.684
	G	7.7239	7.6878	7.7032	7.7655	7.7212	7.7298	7.6998	7.6723	7.6766
	IWP	7.7367	7.6985	7.7143	7.7776	7.7319	7.7407	7.7082	7.6792	7.6837

Table 7 The effect of the length scale on dimensionless fundamental frequency SSSS square nanoplates with different TPMS types, GPL and porosity distributions ($a/h = 20$, $K_w = 75$, $K_s = 25$, $\rho_0 = 0.8$, $\mu = 1$, and $\Lambda_{GPL} = 1$ wt.%)

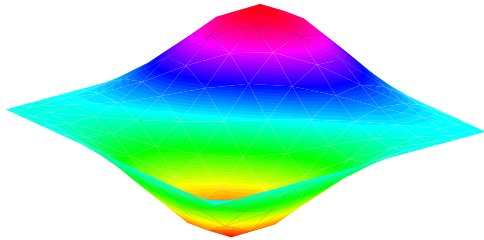
Length scale (l)	Pattern types	PD ₁			PD ₂			PD ₃		
		GPL ₁	GPL ₂	GPL ₃	GPL ₁	GPL ₂	GPL ₃	GPL ₁	GPL ₂	GPL ₃
0	P	6.6777	6.6241	6.6605	6.9497	6.857	6.8871	6.6994	6.6449	6.6510
	G	6.6645	6.6148	6.6486	6.9127	6.8279	6.8556	6.6813	6.6309	6.6367
	IWP	6.6989	6.6410	6.6790	6.9373	6.8515	6.8798	6.6980	6.6445	6.6507
0.5	P	6.6881	6.6322	6.6701	6.9714	6.8751	6.9063	6.7106	6.6538	6.6602
	G	6.6743	6.6224	6.6576	6.9329	6.8448	6.8736	6.6918	6.6392	6.6452
	IWP	6.7102	6.6498	6.6895	6.9585	6.8693	6.8988	6.7093	6.6534	6.6598
1	P	6.7189	6.656	6.6986	7.0351	6.9283	6.9628	6.7440	6.6802	6.6873
	G	6.7034	6.6451	6.6846	6.9923	6.8945	6.9264	6.7228	6.6638	6.6705
	IWP	6.7437	6.6759	6.7204	7.0207	6.9218	6.9544	6.7425	6.6798	6.6869
2	P	6.8370	6.7484	6.8081	7.2720	7.1280	7.1742	6.8717	6.7821	6.7918
	G	6.8154	6.7329	6.7885	7.2145	7.0820	7.1249	6.8421	6.7589	6.7680
	IWP	6.8721	6.7767	6.8391	7.2530	7.1194	7.1632	6.8699	6.7817	6.7914



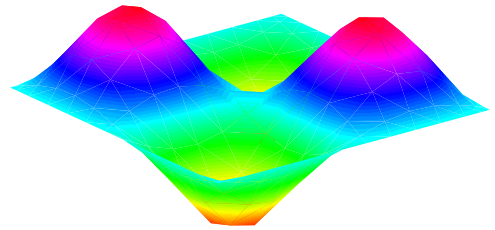
a) Mode 1, $\omega_1^* = 7.5984$



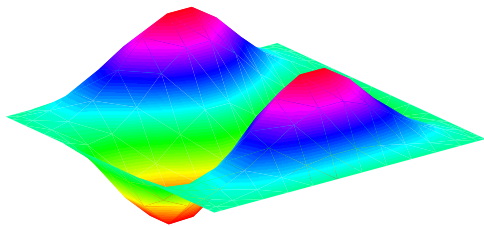
b) Mode 2, $\omega_2^* = 9.6876$



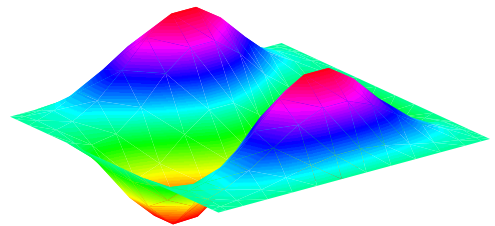
c) Mode 3, $\omega_3^* = 9.6876$



d) Mode 4, $\omega_4^* = 11.1491$



e) Mode 5, $\omega_5^* = 11.8329$



f) Mode 6, $\omega_6^* = 11.8329$

Figure 3 The first six mode shapes of SSSS nanoplates ($a/h = 50, K_w = 50, K_s = 50, \rho_0 = 0.8, \mu = 0, l = 0, \Lambda_{GPL} = 0.8$ wt.%, P type, PD3 and GPL3 distributions)

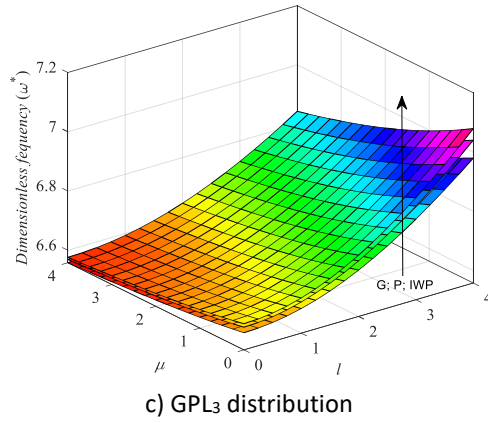
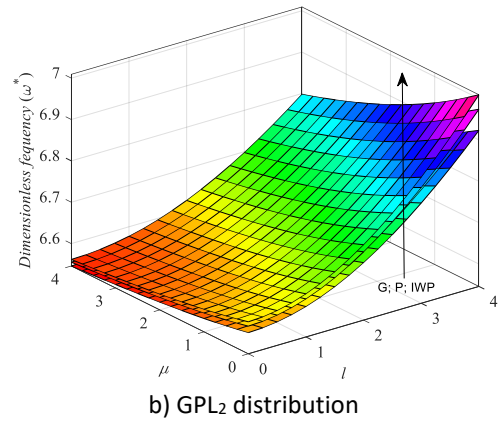
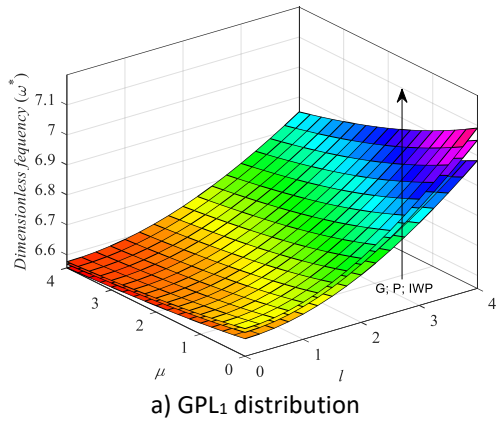


Figure 4 The effect of μ and l parameters on the fundamental frequency of SSS nanoplates with PD₁ distribution ($a/h = 10$, $K_w = 100$, $K_s = 25$, $\rho_0 = 0.9$, and $\Lambda_{GPL} = 0.75$ wt.%)

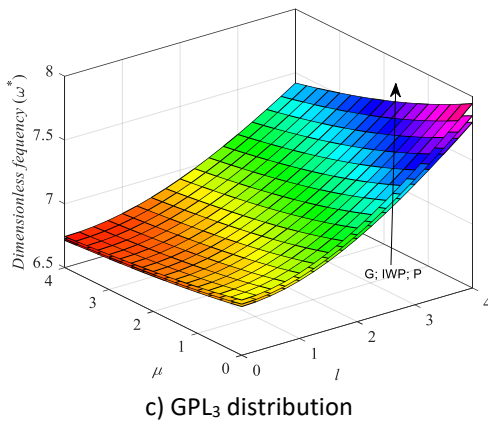
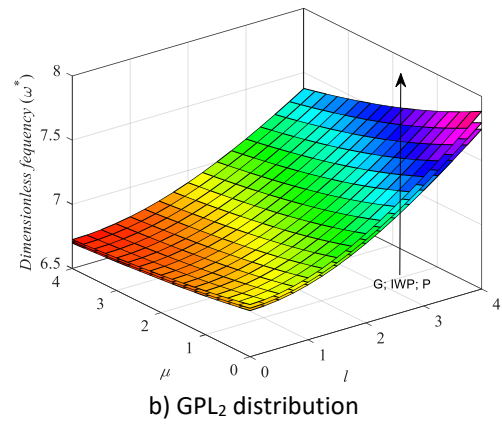
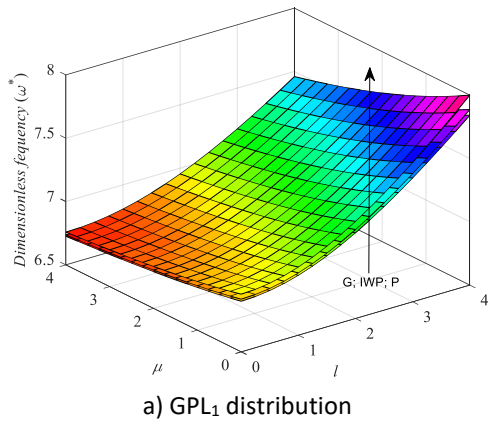
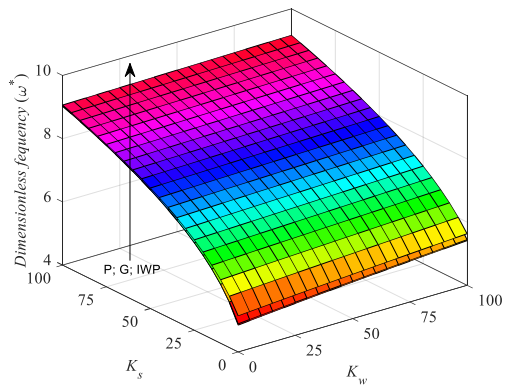
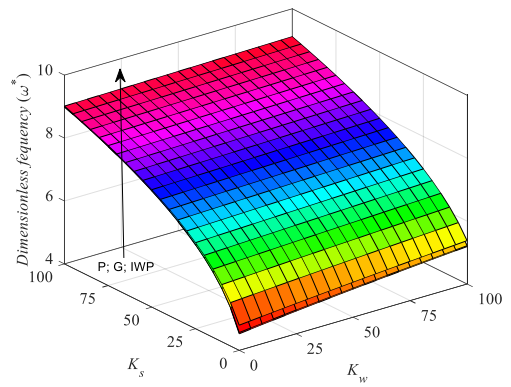


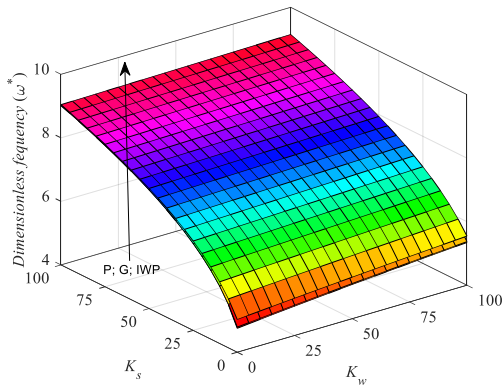
Figure 5 The effect of μ and l parameters on the fundamental frequency of SSS nanoplates with PD₂ distribution ($a/h = 10$, $K_w = 100$, $K_s = 25$, $\rho_0 = 0.9$, and $\Lambda_{GPL} = 0.75$ wt.%)



a) GPL₁ distribution

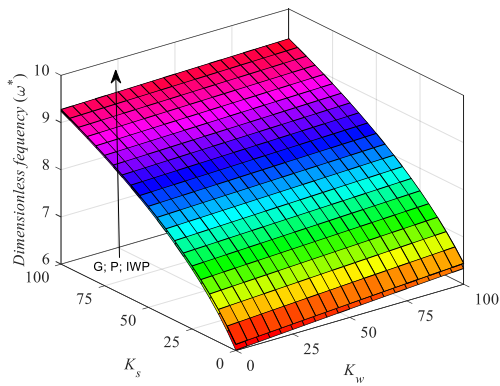


b) GPL₂ distribution

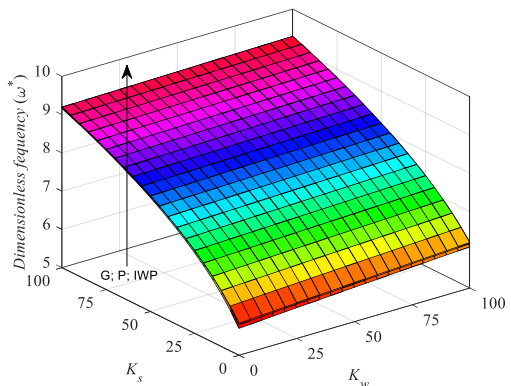


c) GPL₃ distribution

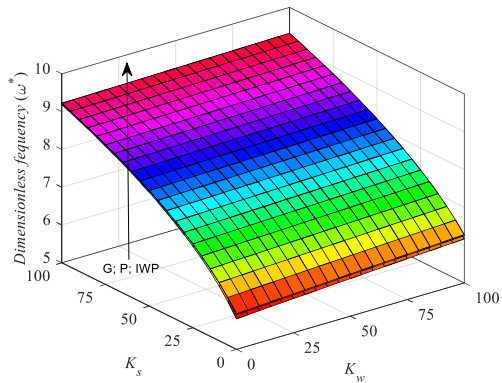
Figure 6 The effect of K_w and K_s parameters on the fundamental frequency of SSS nanoplates with PD₁ distribution ($a/h = 25$, $\rho_0 = 0.8$, $\Lambda GPL = 1$ wt.%, $\mu = 1$ and $l = 1$)



a) GPL₁ distribution



b) GPL₂ distribution



c) GPL₃ distribution

Figure 7 The effect of K_w and K_s parameters on the fundamental frequency of SSS nanoplates with PD₂ distribution ($a/h = 25$, $\rho_0 = 0.8$, $\Lambda GPL = 1$ wt.%, $\mu = 1$ and $l = 1$)

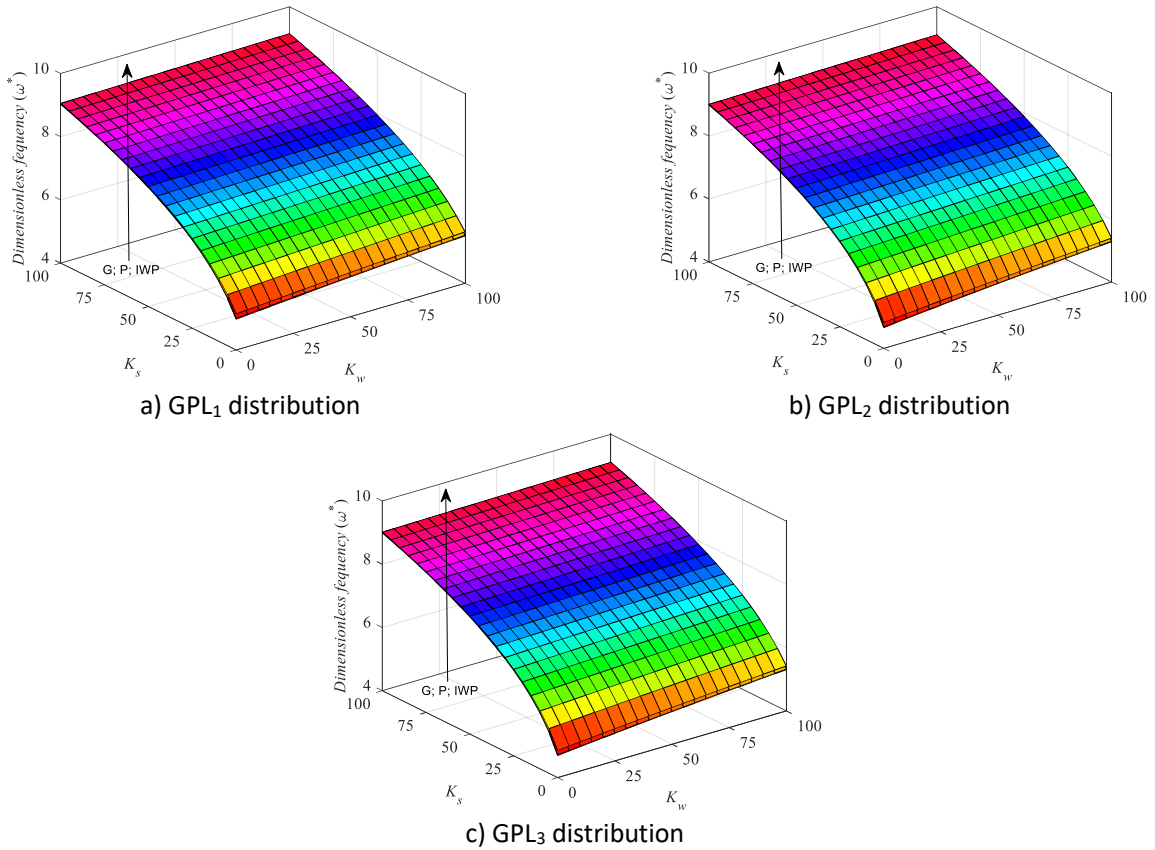


Figure 8 The effect of K_w and K_s parameters on the fundamental frequency of SSS nanoplates with PD₃ distribution ($a/h = 25$, $\rho_0 = 0.8$, $\Lambda GPL = 1$ wt.%, $\mu = 1$ and $l = 1$)

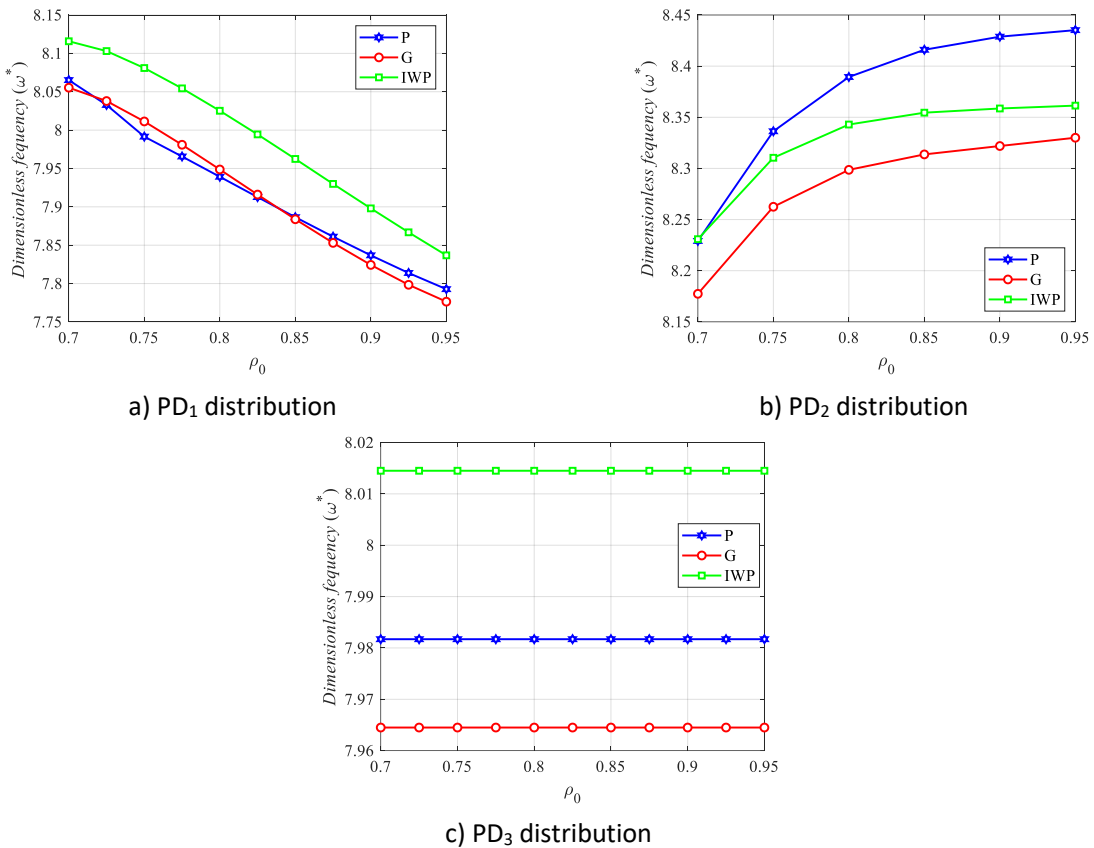


Figure 9 The effect of ρ_0 parameter on the fundamental frequency of CCC nanoplates with GPL₁ distribution ($a/h = 15$, $K_w = K_s = 50$, $\Lambda GPL = 1.2$ wt.%, $\mu = 1$ and $l = 1$)

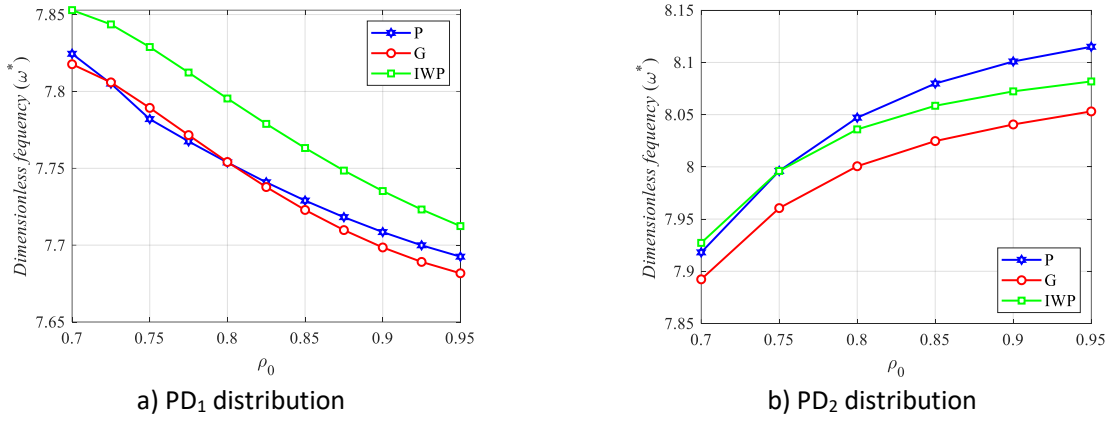


Figure 10 The effect of ρ_0 parameter on the fundamental frequency of SCSC nanoplates with GPL₂ distribution ($a/h = 15, K_w = K_s = 50, \Lambda_{GPL} = 1.2 \text{ wt.}\%, \mu = 1$ and $l = 1$)

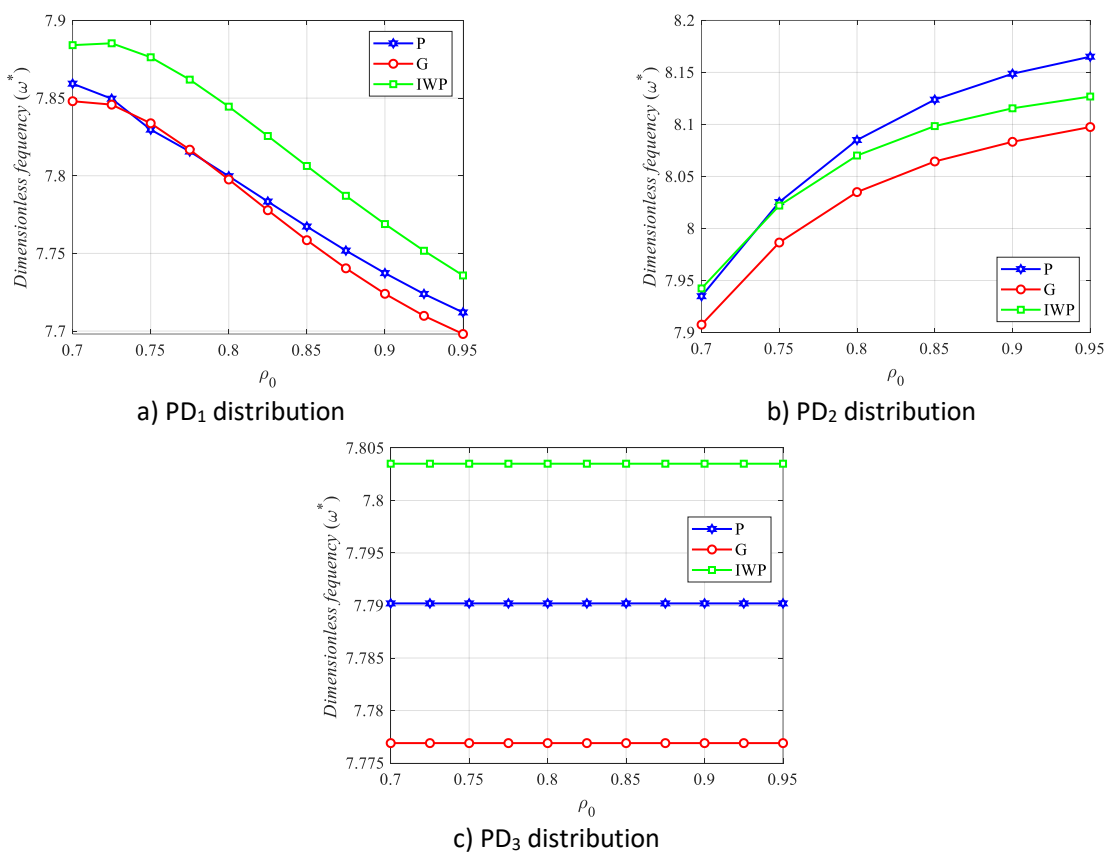
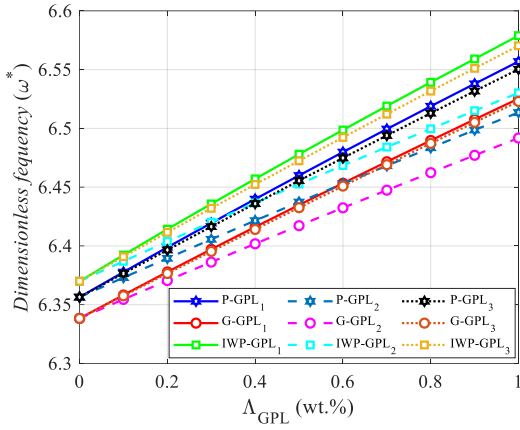
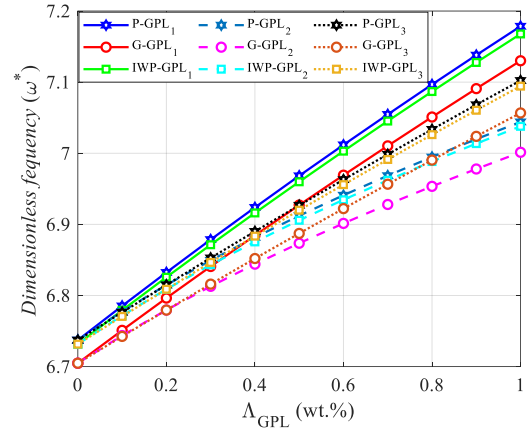


Figure 11 The effect of ρ_0 parameter on the fundamental frequency of SSCC nanoplates with GPL₃ distribution ($a/h = 15, K_w = K_s = 50, \Lambda_{GPL} = 1.2 \text{ wt.}\%, \mu = 1$ and $l = 1$)

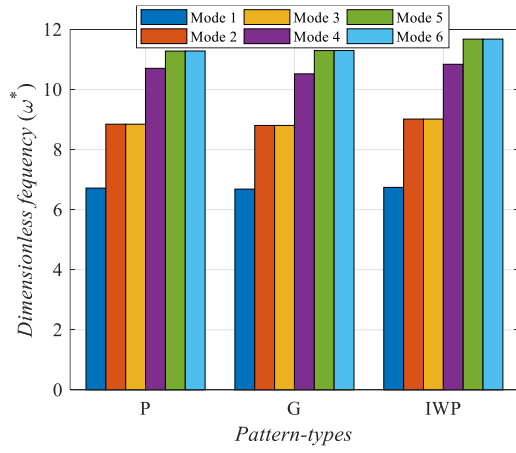


a) PD₁ distribution

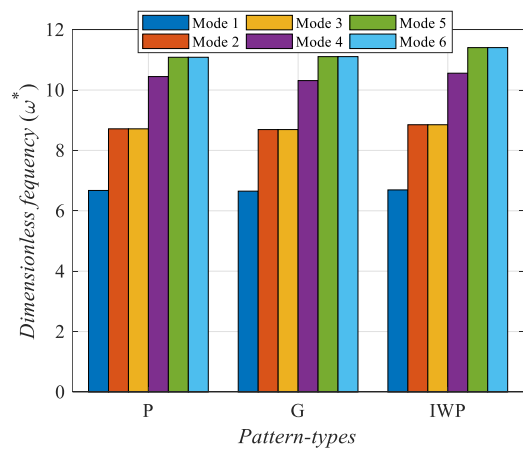


b) PD₂ distribution

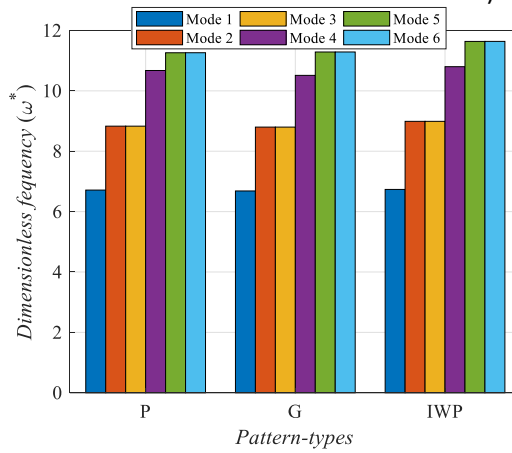
Figure 12 The influence of GPL weight fraction on the fundamental frequency of SSSS nanoplates ($a/h = 40$, $K_w = K_s = 25$, $\mu = 2$, $l = 2$, and $\rho_0 = 0.9$)



a) GPL₁ distribution



b) GPL₂ distribution



c) GPL₃ distribution

Figure 13 The first six fundamental frequencies of SSSS nanoplates with PD₁ distribution ($a/h = 25$, $K_w = 75$, $K_s = 25$, $\mu = 1$, $l = 2$, and $\rho_0 = 0.9$)

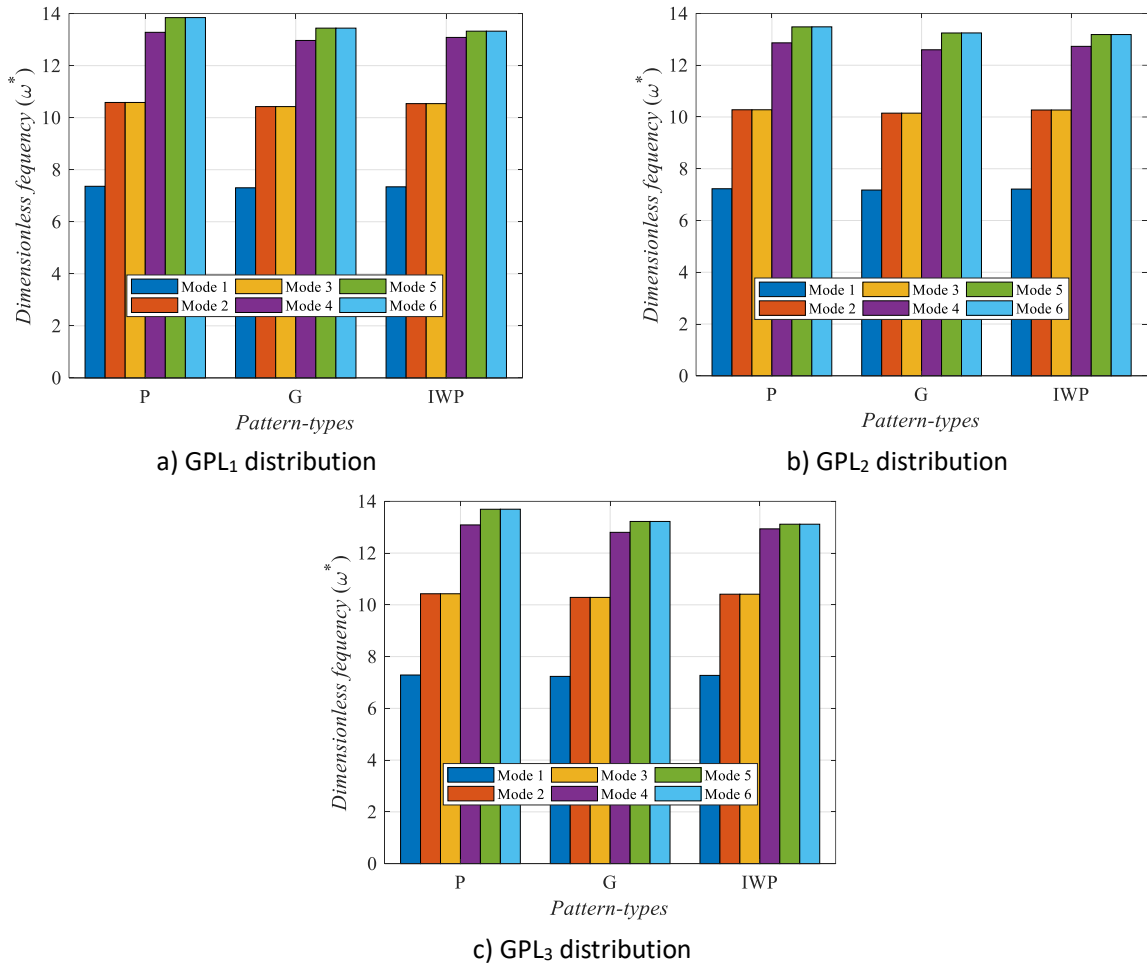


Figure 14 The first six fundamental frequencies of SSSS nanoplates with PD2 distribution ($a/h = 25$, $K_w = 75$, $K_s = 25$, $\mu = 1$, $l = 2$, and $\rho_0 = 0.9$)

5 CONCLUSIONS

This study successfully developed an IGA procedure to study the frequency of GPLR-FG-TPMS nanoplates embedded in PF. To achieve this, an advanced mathematical mechanical model was used. This model used a NURBS-based isogeometric discretization framework based on HSDT and NSGT for accurate displacement approximation. The model allows for the clear observation of the significant influence of the nonlocal factor and length scale on the vibration of GPLR-FG-TPMS nanoplates. Comprehensive parametric studies yielded critical insights, including:

- The proposed numerical model demonstrably captured the vibration characteristics of GPLR-FG-TPMS nanoplates with high accuracy;
- Increasing the nonlocal factor μ leads to a decrease in frequency while increasing the length scale l increases the frequency of the GPLR-FG-TPMS nanoplate;
- The study revealed that for the PD₁ distribution, increasing the porosity parameter leads to a decrease in structural stiffness. Conversely, the PD₂ distribution exhibited the opposite behavior, with stiffness increasing as the porosity parameter grew;
- The addition of GPLs demonstrably enhances the nanoplate stiffness. This effect is particularly evident at low concentrations, where even a small amount of GPLs can significantly strengthen the structure;
- As anticipated, the elastic foundation substantially increases the nanoplate stiffness, resulting in a higher fundamental frequency. Notably, the study revealed that k_s parameter has a more pronounced effect compared to the k_w parameter;

- The numerical results obtained in this study are expected to contribute to the general understanding of GPLR-FG-TPMS nanoplate vibrations as well as open up some potential future research directions such as dynamic problems, nonlinear problems, GPLR-FG-TPMS nanostructure optimization problems, and so on.

Author's Contributions: Writing - Reviewing & Editing, Supervision, Project administration, Methodology, Vo Thanh Tuan; Investigation, Writing Original draft, Software, Ngoc-Tu Do and Nhan Tinh Hoang.

Editor: Pablo Andrés Muñoz Rojas

References

- Al-Ketan, O., & Abu Al-Rub, R. K. (2019). Multifunctional mechanical metamaterials based on triply periodic minimal surface lattices. *Advanced Engineering Materials*, *21*(10), 1900524.
- Ansari, E., & Setoodeh, A. (2020). Applying isogeometric approach for free vibration, mechanical, and thermal buckling analyses of functionally graded variable-thickness blades. *Journal of Vibration and Control*, *26*(23-24), 2193-2209.
- Ansari, E., Setoodeh, A., & Rabczuk, T. (2020). Isogeometric-stepwise vibrational behavior of rotating functionally graded blades with variable thickness at an arbitrary stagger angle subjected to thermal environment. *Composite Structures*, *244*, 112281.
- Arash, B., & Wang, Q. (2011). Vibration of single-and double-layered graphene sheets.
- Arefi, M., & Zenkour, A. M. (2017). Thermo-electro-mechanical bending behavior of sandwich nanoplate integrated with piezoelectric face-sheets based on trigonometric plate theory. *Composite Structures*, *162*, 108-122.
- Daikh, A. A., Draï, A., Bensaid, I., Houari, M. S. A., & Tounsi, A. (2021). On vibration of functionally graded sandwich nanoplates in the thermal environment. *Journal of Sandwich Structures & Materials*, *23*(6), 2217-2244.
- Daikh, A. A., & Zenkour, A. M. (2020). Bending of functionally graded sandwich nanoplates resting on pasternak foundation under different boundary conditions. *Journal of Applied and Computational Mechanics*, *6*(Special Issue), 1245-1259.
- Eringen, A. C. (1972). Nonlocal polar elastic continua. *International journal of engineering science*, *10*(1), 1-16.
- Eringen, A. C. (1983). On differential equations of nonlocal elasticity and solutions of screw dislocation and surface waves. *Journal of applied physics*, *54*(9), 4703-4710.
- Fleck, N., & Hutchinson, J. (1993). A phenomenological theory for strain gradient effects in plasticity. *Journal of the Mechanics and Physics of Solids*, *41*(12), 1825-1857.
- González-Castaño, M., Baena-Moreno, F., De Miguel, J. C. N., Miah, K. U., Arroyo-Torralvo, F., Ossenbrink, R., . . . Wenka, A. (2022). 3d-printed structured catalysts for co2 methanation reaction: Advancing of gyroid-based geometries. *Energy Conversion and Management*, *258*, 115464.
- Hughes, T. J., Cottrell, J. A., & Bazilevs, Y. (2005). Isogeometric analysis: Cad, finite elements, nurbs, exact geometry and mesh refinement. *Computer methods in applied mechanics and engineering*, *194*(39-41), 4135-4195.
- Keshtegar, B., Motezaker, M., Kolahchi, R., & Trung, N.-T. (2020). Wave propagation and vibration responses in porous smart nanocomposite sandwich beam resting on kerr foundation considering structural damping. *Thin-Walled Structures*, *154*, 106820.
- Li, C., Lai, S., & Yang, X. (2019). On the nano-structural dependence of nonlocal dynamics and its relationship to the upper limit of nonlocal scale parameter. *Applied Mathematical Modelling*, *69*, 127-141.
- Li, C., Zhu, C., Zhang, N., Sui, S., & Zhao, J. (2022). Free vibration of self-powered nanoribbons subjected to thermal-mechanical-electrical fields based on a nonlocal strain gradient theory. *Applied Mathematical Modelling*, *110*, 583-602.

- Liew, K., He, X., & Wong, C. (2004). On the study of elastic and plastic properties of multi-walled carbon nanotubes under axial tension using molecular dynamics simulation. *Acta Materialia*, 52(9), 2521-2527.
- Lim, C., Zhang, G., & Reddy, J. (2015). A higher-order nonlocal elasticity and strain gradient theory and its applications in wave propagation. *Journal of the Mechanics and Physics of Solids*, 78, 298-313.
- Lu, P., Zhang, P., Lee, H., Wang, C., & Reddy, J. (2007). Non-local elastic plate theories. *Proceedings of the Royal Society A: Mathematical, Physical and Engineering Sciences*, 463(2088), 3225-3240.
- Nguyen-Xuan, H., Tran, K. Q., Thai, C. H., & Lee, J. (2023). Modelling of functionally graded triply periodic minimal surface (fg-tpms) plates. *Composite Structures*, 315, 116981.
- Nguyen, N. V., Tran, K. Q., & Nguyen-Xuan, H. (2024). A refined quasi-3d isogeometric nonlinear model of functionally graded triply periodic minimal surface plates. *Engineering with Computers*, 40(4), 2161-2181.
- Nguyen, N. V., Tran, K. Q., Phung-Van, P., Lee, J., & Nguyen-Xuan, H. (2023). An isogeometric analysis of functionally graded triply periodic minimal surface microplates. *Aerospace Science and Technology*, 137, 108270.
- Nguyen, Q. H., Nguyen, L. B., Nguyen, H. B., & Nguyen-Xuan, H. (2020). A three-variable high order shear deformation theory for isogeometric free vibration, buckling and instability analysis of fg porous plates reinforced by graphene platelets. *Composite Structures*, 245, 112321.
- Phung-Van, P., Thai, C. H., Abdel-Wahab, M., & Nguyen-Xuan, H. (2020). Optimal design of fg sandwich nanoplates using size-dependent isogeometric analysis. *Mechanics of Materials*, 142, 103277.
- Rafiee, M. A., Rafiee, J., Wang, Z., Song, H., Yu, Z.-Z., & Koratkar, N. (2009). Enhanced mechanical properties of nanocomposites at low graphene content. *ACS nano*, 3(12), 3884-3890.
- Reddy, J. N. (1984). A simple higher-order theory for laminated composite plates.
- Sankineni, R., & Ravi Kumar, Y. (2022). Evaluation of energy absorption capabilities and mechanical properties in fdm printed pla tpms structures. *Proceedings of the Institution of Mechanical Engineers, Part C: Journal of Mechanical Engineering Science*, 236(7), 3558-3577.
- Singh, D., Sharma, S., Kumar, R., & Vaish, R. (2023). Representative volume element model of triply periodic minimal surfaces (tpms)-based electrostrictive composites for numerical evaluation of effective properties. *Acta Mechanica*, 234(2), 355-375.
- Sobhy, M., & Radwan, A. F. (2017). A new quasi 3d nonlocal plate theory for vibration and buckling of fgm nanoplates. *International Journal of Applied Mechanics*, 9(01), 1750008.
- Soldatos, K. (1992). A transverse shear deformation theory for homogeneous monoclinic plates. *Acta Mechanica*, 94(3), 195-220.
- Stölken, J. S., & Evans, A. (1998). A microbend test method for measuring the plasticity length scale. *Acta Materialia*, 46(14), 5109-5115.
- Thai, C. H., Ferreira, A., Nguyen-Xuan, H., Nguyen, L. B., & Phung-Van, P. (2023). A nonlocal strain gradient analysis of laminated composites and sandwich nanoplates using meshfree approach. *Engineering with Computers*, 1-17.
- Thai, C. H., Ferreira, A., & Phung-Van, P. (2020). A nonlocal strain gradient isogeometric model for free vibration and bending analyses of functionally graded plates. *Composite Structures*, 251, 112634.
- Toupin, R. (1962). Elastic materials with couple-stresses. *Archive for rational mechanics and analysis*, 11(1), 385-414.
- Tran, K. Q., Hoang, T.-D., Lee, J., & Nguyen-Xuan, H. (2024). Three novel computational modeling frameworks of 3d-printed graphene platelets reinforced functionally graded triply periodic minimal surface (gplr-fg-tpms) plates. *Applied Mathematical Modelling*, 126, 667-697.
- Zeighampour, H., & Shojaeian, M. (2019). Buckling analysis of functionally graded sandwich cylindrical micro/nanoshells based on the couple stress theory. *Journal of Sandwich Structures & Materials*, 21(3), 917-937.
- Zhao, M., Li, X., Zhang, D. Z., & Zhai, W. (2023). Tpms-based interpenetrating lattice structures: Design, mechanical properties and multiscale optimization. *International Journal of Mechanical Sciences*, 244, 108092.

